Received: 14 July 2020 | Accepted: 27 October 2020

DOI: 10.1111/jace.17570

ORIGINAL ARTICLE

Journal of the American Ceramic Society

t-ZrO_2 toughened Al_2O_3 free-standing films and as oxidation mitigating thin films on silicon nitride via colloidal processing of flame made nanopowders (NPs)

Xinyu Zhang[1] | **Xiaopo Cheng**[1] | **Monika Jansohn**[1] | **Matthias Niedermaier**[1,2] | **Thomas Lenk**[1,3] | **Stefan Britting**[4] | **Karsten Schmidt**[4] | **Richard M. Laine**[1]

[1]Materials Science and Engineering, University of Michigan, Ann Arbor, MI, USA

[2]Chemistry and Physics of Materials, Paris-Lodron University of Salzburg, Salzburg, Austria

[3]Professorship of Chemical Technology, Chemnitz University of Technology, Chemnitz, Germany

[4]Rogers Germany GmbH, Eschenbach in der Oberpfalz, Germany

Correspondence
Richard M. Laine, Materials Science and Engineering, University of Michigan, Ann Arbor, MI 48109-2136, USA.
Email: talsdad@umich.edu

Funding information
Rogers Corporation

Abstract

Zirconia toughened aluminas (ZTAs) are one of the most important engineering ceramics with high melting points, excellent mechanical strength, and chemical stability, and are commonly used as wear resistant and high-temperature components, as prosthetic implants, and electric circuit substrates. In this work, we explore methods of processing fine-grained, dense, thin, free-standing $(ZrO_2)_x(Al_2O_3)_{1-x}$ films (x = 0-50 mol%, ~40 μm thick) by sintering flame made nanopowders (NPs) to optimize the t-ZrO_2 content, sinterability, and microstructures under select conditions (1120°C-1500°C/5 h in O_2 or 95%N_2/5%H_2). In all cases, the final sintered products retain t-ZrO_2 with average grain sizes (AGSs) of 0.1-1 μm. ZTA film thicknesses were increased to ~200 μm to assess potential as electronic substrates. Excellent fracture toughness (24 MPa $m^{1/2}$) and small AGSs of 0.7 μm were found for ~200 μm thick ZTA films sintered at 1500°C/5 h/N_2/H_2 using a three-step binder burnout process. Furthermore, we show that homogeneous ZTA thin films (<5 μm thick) can be sintered on Si_3N_4 substrates (thickness ≈ 300 μm) to provide physical protection against oxidation under extreme conditions (1500°C/1 h/O_2), offering additional practical utility for high-temperature ceramics and power electronic substrates.

KEYWORDS

alumina, LF-FSP, nanoparticles, nanopowders, nitrides, power electronic substrates, Si_3N_4, sinter/sintering, tetragonal zirconia, zirconia, ZTA

1 | INTRODUCTION

Alumina (Al_2O_3) is a widely studied structural ceramic with applications as grinding media, for cutting tools, high-temperature engine components, prosthetic implants, and substrates for power electronics due to its high melting point, excellent mechanical strength, hardness, and chemical stability as well as its widespread abundance.[1–17] However, applications using pure α-Al_2O_3 are limited by its low resistance to crack propagation, that is, poor fracture toughness (4-5 MPa $m^{1/2}$)[18,19] that can lead to catastrophic failure.[1–3] To enhance Al_2O_3 fracture toughness, a common practice involves incorporating additives, such as tetragonal zirconia (t-ZrO_2), to increase toughness while maintaining the hardness and chemical resistance of Al_2O_3, commonly referred to as zirconia toughened aluminas (ZTAs).[2–6,20–29]

Room-temperature stabilized t-ZrO_2 will transform to monoclinic (m-ZrO_2) if subjected to mechanical stress. This transformation is accompanied by a 4% volume expansion creating a compressive stress field in the surrounding grains, which opposes crack propagation.[2–4,20–24] In this process, some fraction of the energy needed for crack propagation

is consumed by promoting the $t \rightarrow m$ transformation, the operative mechanism that inhibits crack propagation.[21–24] Unfortunately, t-ZrO_2 typically transforms to m-ZrO_2 at 950°C-1000°C on cooling making it unstable at lower temperatures.[2–4,20–24] A resolution to this problem is to stabilize t-ZrO_2 by introducing dopants with cationic radii close to that of Zr^{4+} (0.8-1 Å, eg, Y^{3+}, Ca^{2+}, Mg^{2+}, and related rare earth ions).[2,6–8,21–23,26,30–33] Table 1 compares various ZTA compositions synthesized/sintered using different methods and their selected properties. In general, yttria (Y^{3+}) is the most common dopant, stabilizing t-ZrO_2 after sintering at 1600°C/1-5 h/air (Table 1).[2,6,21]

Previously, we demonstrated that it is possible to sinter flame made nanopowders (NPs, average particle sizes, APSs: 40-60 nm) consisting of particles of t-ZrO_2 encapsulated within δ-Al_2O_3 shells to fully dense $(t\text{-}ZrO_2)_{0.54}(\alpha\text{-}Al_2O_3)_{0.46}$ pellets (diameter = 13 mm; thickness = 1.4 mm) with AGSs ≤ 200 nm at 1120°C/6 h/air. The encapsulation process seems to stabilize the t-ZrO_2 without the need for additives likely due to rapid quenching of the flame made NPs (liquid-feed flame spray pyrolysis, LF-FSP) to kinetically rather than thermodynamically stable phases produced using traditional processing methods.[27–29]

We have recently returned to these flame made NPs, demonstrating their utility as a simple and scalable route to functional ceramic thin films (< 100 μm thick) for applications such as capacitors, solid electrolytes, and electrodes for solid-state batteries.[34–36] Coincidentally, we reported processing dense and flexible α-Al_2O_3 thin films (< 10 μm).[10]

Our success with α-Al_2O_3 thin films prompted efforts to extend our new approach to t-ZrO_2-doped α-Al_2O_3 thin films targeting mechanical properties superior to α-Al_2O_3 for applications including electronic substrates and protective coatings.

In the first part of the present work, we explored sintering $(ZrO_2)_x(Al_2O_3)_{1-x}$ thin films (x = 0-50 mol%, ~40 μm thick) using a select set of conditions (1120°C-1500°C/5 h in O_2 or 95%N_2/5%H_2) from NPs by LF-FSP to optimize ZrO_2 content, sinterability, and microstructures. Similar to our previous work,[27–29] all films retain t-ZrO_2 at RT with AGSs of 0.1-1 μm.

Although no t-ZrO_2 stabilizing additives are needed due to rapid quenching of LF-FSP, additives such as TiO_2 and MgO were found to be effective in tailoring final grain sizes and sinterability, permitting us to optimize the ZTA composite properties. Studies show that TiO_2 doping enhances densification and reduces ZTA sintering temperatures on substituting Al^{3+} by Ti^{4+} which generates vacancies, thereby improving diffusion.[7,37–40] Additionally, Chen et al[7,8] report the formation of a liquid phase at ZTA grain boundaries with TiO_2 contents ≥ 4 wt%, which also promotes densification. Unfortunately, TiO_2 doping sometimes coincides with excessive grain growth leading to a reduced elastic modulus and hardness.[7,8,37] Consequently,

TABLE 1 Comparison of ZTA ceramics in literature and this work

ZrO_2 (%)[a]	t (%)[b]	Powder processing/ synthesis	Sintering condition (°C/h)	AGS (μm)[c]	Relative density (%)	Mechanical properties[d]	References
5-20 vol	10-90	Ball milling	1500/2, hot-pressing	0.4-5	—	K_{1C}: 6-8 H_v: 10-12	[20]
5-30 vol (3Y)	50-100	Ball milling	1600/1/air	0.3-3	96-99	E: 340-390 σ: 400-950	[21]
5 mol	75	Sol-gel	1550/4/air	0.1-4	98	E: 370 K_{1C}: 5 H_v: 17	[4,5]
30 wt (3Y)	100	GCHAS[e]	1600/1/air	0.6-4	92	K_{1C}: 5.5 H_v: 14-15 σ: 610	[6]
20 wt (10M)	25	Ball milling	1600/2/air	~1	94.5	K_{1C}: 11.5 H_v: 16.4	[23]
10-30 wt(3Y)	8-25	Co-precipitation	1600/5/air	0.5-3	96-98	K_{1C}: 8-8.5	[2]
54 mol	100	LF-FSP	1120/6/air	~0.2	99	—	[27–29]
10 mol[f]	100	LF-FSP	1500/5/N_2/H_2	0.5-1	97-99	K_{1C}: 24	This work

[a]ZrO_2 content, t-ZrO_2 stabilizing additives: 3Y = 3 mol.% Y_2O_3, 10M = 10 wt.% MgO.

[b]t-ZrO_2 content in sintered ceramics at room temperature.

[c]Average grain sizes of both Al_2O_3 and ZrO_2.

[d]K_{1C}: fracture toughness (MPa $m^{1/2}$); H_v: Vickers hardness (GPa); E: elastic modulus (GPa); σ: flexural strength (MPa).

[e]Gel casting hydrolysis-assisted solidification.

[f]One example is given: 10 mol.% ZrO_2-doped Al_2O_3 films (~200 μm thick) with MgO and TiO_2 (1 wt.% each).

we sought to eliminate this issue by introducing MgO, which is quite useful in limiting grain sizes in the α-Al_2O_3 thin films.

MgO is known to be an effective additive in inhibiting grain growth during sintering through segregation of MgO-Al_2O_3 solid solutions (solubility limit ≈500 ppm MgO) and/or pinning through formation of fine spinel particles ($MgAl_2O_4$) at grain boundaries resulting in reduced grain boundary mobility.[10,40–51] It has also been suggested that the dominant densification mechanism is via surface diffusion for MgO doping levels of 0.1-0.3 wt.%, and grain boundary diffusion for MgO concentrations of 0.5-1.0 wt%.[47,48] In this work, both TiO_2 and MgO additives (~1 wt% each) were used to optimize sinterability and final microstructures.

While thin films are suitable for applications such as electronic devices and protective coatings, for other structural applications such as wear components, dental composites, and prosthetic implants, bulk materials are also highly desirable. At the interface between bulk and thin films, intermediate thicknesses, for example, up to ~300 μm, are used as electrically insulating layers as well as high-strength substrates for piezoresistive sensors and power electronics.[11–14] Finally, to test ZTA mechanical properties, greater thicknesses are preferred to prevent cracking caused simply by handling.

These issues provided the motivation to expand our approach to ZTA films up to ~200 μm thick and up to ~2 × 2 cm^2. To our surprise, ~200 μm thick ZTA films doped with MgO and TiO_2 (1 wt% each) show a fracture toughness of 24 MPa $m^{1/2}$ using SEPB, which is two to four times higher than the reported values (Table 1), suggesting potential application as electronic substrates with improved mechanical properties.

Similar to ZTA films, silicon nitride (Si_3N_4) films (~300 μm thick) are also commonly used in structural applications due to their good chemical, physical and thermal stabilities, and mechanical properties.[15,16,52–58] For electronic substrates, Si_3N_4 films exhibit superior thermal conductivity (κ) of ~90 W/mK (at RT) and a K_{1C} of 6.5-7 MPa $m^{1/2}$ compared to ZTA films (typically $\kappa = 28$ W/mK and $K_{1C} \approx 5$ MPa $m^{1/2}$), providing better thermal conductivity and reliability.[15,57]

Unfortunately, Si_3N_4 is susceptible to oxidation even at ambient and may deteriorate over time.[52–55] Although a surface oxide/oxynitride layer that forms can protect against further oxidation,[52,53] to withstand high-temperature oxidation and/or active oxidation environments, additional protection is needed. In the present work, we find that sintered ZTA coatings (<5 μm) adhere well to Si_3N_4 substrates (thickness ≈ 300 μm) providing physical protection against oxidation after heating to 1500°C/1 h/O_2 as characterized by scanning electron microscope (SEM).

2 | EXPERIMENTAL PROCEDURES

2.1 | Precursor syntheses

Nanopowders were produced by liquid-feed flame spray pyrolysis (LF-FSP), which was invented in the Laine group at the University of Michigan. It is a single-step continuous synthesis method for producing ceramic NPs. Typical metallo-organic precursors in this work include metal-carboxylates and metal-atrane compounds; detailed synthesis procedures are reported elsewhere.[10,27–29,34–36,59–62] Representative examples are provided in the Supporting Information (S1).

2.2 | Liquid-Feed Flame Spray Pyrolysis (LF-FSP)

Metallo-organic precursors at selected compositions were dissolved in alcohol, usually ethanol, at 1-10 wt% solid loading. The solution is fed (30-80 ml min^{-1}) into an atomizing nozzle (BETE XA-PR) and aerosolized with oxygen (80 psi, 40 ml min^{-1}) into a quartz chamber where it is ignited with methane/oxygen (40 ml min^{-1}/30 ml min^{-1}) pilot torches on the spray head. Oxygen shield gas (150 ml min^{-1}) provides an oxygen-rich environment to minimize carbon residues. Initial combustion takes place producing temperatures of ≥ 1500°C followed by a quenching step that drops the temperature to 300°C-500°C over 1.5 m, equivalent to a 1000°C quench in < 100 ms, to produce NPs. Powders are collected downstream in rod-in-tube electrostatic precipitators (ESP) operating at 10 kV. Scheme 1 illustrates the LF-FSP apparatus for NP production.

As-produced NPs were then dispersed in ethanol (200 proof, Decon Labs) using an ultrasonic horn (Vibra cell VC-505, Sonics & Materials Inc Newtown) at 100 W/10 min. The suspension was allowed to settle for 5 h to remove larger particles. The supernatant was decanted and allowed to oven dry (60°C/12 h) providing the starting ZrO_2-doped δ-Al_2O_3 NPs.

2.3 | Film processing

Generally, LF-FSP-synthesized NPs were mixed with polymeric additives such as binder, plasticizer, curing agent, and dispersant, in a selected solvent system by ball-milling (Rotary Tumbler Model B, Tru-Square Metal Products) using 3.0 mm diameter spherical Al2O3 as the milling media. One-fifth of the container (20 ml) was filled with the milling media (~6 g). An example suspension of ZrO_2-doped Al_2O_3 is given in Table S1.

The suspensions were cast on Mylar film using a wire-wound rod coater (Automatic Film Applicator-1137, Sheen Instrument, Ltd.). The cast thickness was adjusted to 100-255 μm to control the thickness of the final ceramic film.

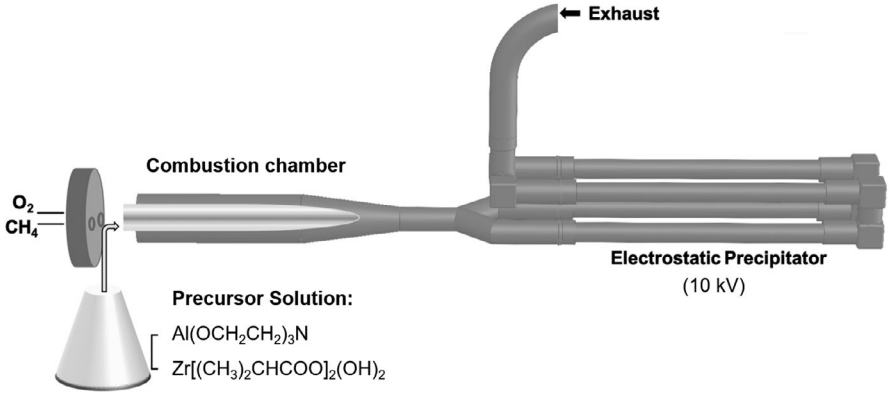

SCHEME 1 Liquid-feed flame spray pyrolysis (LF-FSP) for nanopowder production

A glass cover was used to control the solvent drying rate to avoid mud cracking.

After solvents evaporated, dried green films were uniaxially pressed between stainless steel dies at 100°C at 10 ksi/5-30 min using a heated benchtop laboratory manual press (Model 3851-0, Carver, Inc) to improve packing density.[10,34–36] One/two layers for thin films (thickness ≈ 20-80 μm) and 8-10 layers for thick films (thickness ≈ 200 μm) were pressed together.

2.4 | Film sintering

Green films (typically 5 × 5 mm^2) were placed between two Al_2O_3 substrates (diameter = 42 mm) and sintered to selected temperatures, times, and ramp rates, using a vacuum tube furnace (GSL-1600X). The substrates were used to prevent warping of the ceramic films.

Films were subject to binder burnout process prior to sintering by heating them to 800°C/1 h in extra dry grade O2 (60 ml min^{-1}). Subsequently, they were sintered at various conditions: 1120°C-1500°C at 1°C-10°C min^{-1} under a constant gas (O2 or 95%N_2/5%H_2) flow of 60 ml min^{-1}. For convenience, 95% N_2/5% H_2 is referred to as N_2/H_2 in the following sections. Typical sintering schedules are given in Figure S1.

2.5 | Coating Si_3N_4 substrates

Suspensions of 10 mol% ZrO_2-doped δ-Al_2O_3 for coating Si_3N_4 substrates (Rogers Corp.) were prepared per Table S2.

Si_3N_4 films were coated one side at a time. The suspension was first cast on one side of Si_3N_4 samples with 25 μm spacers using the coating setup shown in Figure S2; then the films were thermally pressed at 100°C bottom, 60°C top, 8 ksi. They were sintered in two steps: binder burnout at 800°C/1 h/O_2; and sintering at 1500°C/5 h/N_2/H_2 (Figure S1B). The other side of the films was then coated and sintered following the same procedure.

3 | RESULTS AND DISCUSSIONS

In the following sections, we first characterize microstructures, sinterability, and phase compositions of ZTA thin films (~40 μm) derived from $(ZrO_2)_x(Al_2O_3)_{1-x}$ (x = 0-50 mol%) NPs sintered under select conditions. Film thicknesses were then increased to ~200 μm to explore their potential utility as substrates for power electronics. The effects of different sintering conditions were explored to minimize cracking

TABLE 2 Selected properties of $(ZrO_2)_x(Al_2O_3)_{1-x}$ (x = 0, 15, 30, 50 mol%) nanopowders

ZrO_2 content, mol.%	ZrO_2 content, wt%	Density*, g/cm^3	SSA, m^2/g	APS, nm
0	0	3.95	49 ± 0.5	31 ± 0.3
15	17.6	4.25	50 ± 0.5	28 ± 0.3
30	34.1	4.54	53 ± 0.5	25 ± 0.2
50	54.7	4.90	40 ± 0.3	30 ± 0.3

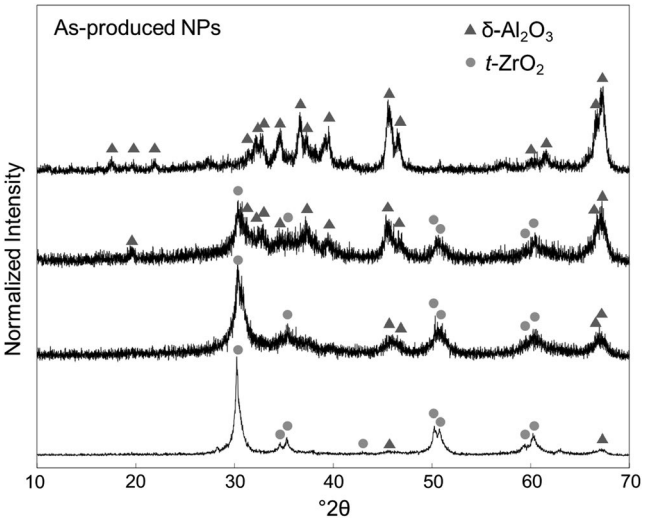

FIGURE 1 XRDs of $(ZrO_2)_x(Al_2O_3)_{1-x}$ (x = 0, 15, 30, and 50 mol%) NPs

while optimizing microstructures and densities. Finally, ZTA coatings on Si_3N_4 substrates were processed and optimized as characterized by a dye penetration test, an oxygen damage test, XRD, and SEM.

4 | ZTA ~40 μm THIN FILMS

To identify the mix of phases required to optimize the properties of the final sintered products, $(ZrO_2)_x(Al_2O_3)_{1-x}$ (x = 0, 15, 30, 50 mol%) NPs were produced by LF-FSP. APSs and specific surface areas (SSAs) were calculated using BET data (see experimental) per Table 2. All NPs show similar SSAs of 40-50 m^2/g and APSs of ~30 nm; $(ZrO_2)_{0.3}(Al_2O_3)_{0.7}$ shows the lowest APS of 25 nm. Figure S3 shows SEMs of as-produced Al_2O_3 and $(ZrO_2)_{0.5}(Al_2O_3)_{0.5}$ NPs, both exhibit a broad size distribution with APSs <50 nm, and a few particles >100 nm that are likely agglomerated in overall agreement with Table 2 APSs. Nanosized powders with log normal particle size distributions are advantageous for processing in that they reduce sintering temperatures due to high surface energies and provide high packing densities.

Figure 1 compares XRDs of as-produced $(ZrO_2)_x(Al_2O_3)_{1-x}$ NPs. As produced LF-FSP Al_2O_3 is a mixture of δ-Al_2O_3 phases, as expected from previous work.[10,27,59] For ZrO_2 (x > 0 mol.%)-doped Al_2O_3, a mixture of δ-Al_2O_3 and t-ZrO_2 is observed, as previously reported for $(t\text{-}ZrO_2)_x(\delta\text{-}Al_2O_3)_{1-x}$ (x = 0.02-0.8) core-shell NPs.[27–29]

Figure 2 compares SEMs of $(ZrO_2)_x(Al_2O_3)_{1-x}$ thin films (40-60 μm thick) sintered under different conditions in O_2 (see Figure S1A schedule). All films show uniform grain sizes (100-500 nm, Figure 3), and densities increase with the

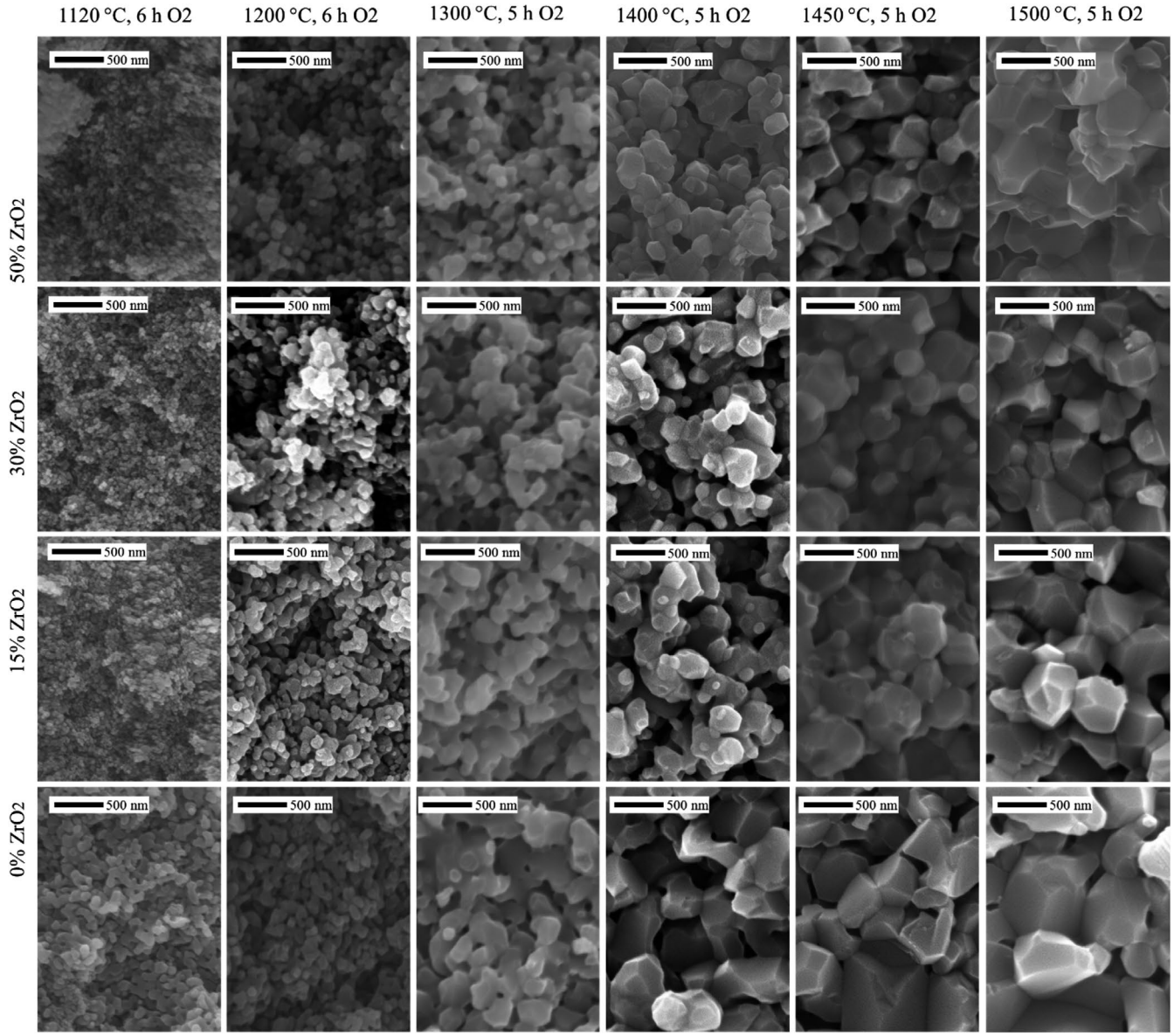

FIGURE 2 SEM fracture surfaces of sintered $(ZrO_2)_x(Al_2O_3)_{1-x}$ (x = 0, 15, 30, 50 mol%) thin films

sintering temperature, but pores are not fully eliminated even at 1500°C.

Figure 3A suggests that grain sizes decrease slightly with increasing ZrO_2 content, although the difference for higher contents is not significant. As seen in Figure 3B, film thicknesses decrease with increasing sintering temperature. Overall, the 30 mol% ZrO_2 film shows the smallest final AGSs and the greatest decrease in thickness at higher temperatures.

Previous reports indicate that sintering α-Al_2O_3 in a hydrogen atmosphere improves densification and reduces porosity.[10,63] These results prompted efforts here to sinter thin $(ZrO_2)_x(Al_2O_3)_{1-x}$ (x = 15, 30, and 50 mol%) films in N_2/H_2 following a two-step procedure per Figure S1B: binder burnout at 800°C/1 h/O_2 and sintering at 1400°C/5 h/N_2/H_2. As shown in Figure S4, compared to films sintered in O_2 (Figure 2), an N_2/H_2 atmosphere improves densification slightly, and AGSs appear to be smaller. However, the films are porous suggesting incomplete densification.

As demonstrated in Figures 2 and 3, 30 mol.% ZrO_2-doped Al_2O_3 films show limited grain growth and the most significant decrease in thickness on sintering at 1400°C-1500°C compared to other compositions. As discussed in the introduction, TiO_2 doping improves Al_2O_3 densification but increases grain sizes,[7,8,37–40] while MgO limits grain growth.[10,40–51] Therefore, to further improve sinterability, the effects of TiO_2 and MgO additives (1 wt% each) to 30 mol% ZrO_2-doped Al_2O_3 were investigated.

As seen in Table 3, we studied the sintering effects of two different TiO_2 powders (1 wt% doping): TiO_2 commercial powder (CP, claimed APS ≈20 nm), and TiO_2 NP by LF-FSP (APS = 20-30 nm). For composition **D**, MgO doping was introduced by mixing LF-FSP-produced 30 mol% ZrO_2-doped Al_2O_3 and 2 wt% MgO-doped Al_2O_3 NPs, the resulting mixture has a 10 mol% ZrO_2 and ~1 wt% MgO content. MgO (2 wt%)-doped Al_2O_3 NP was chosen based on the work by Takeuchi et al[10] that generated dense and flexible sintered thin films (<10 μm). The ZrO_2 content was reduced because typical power electronic ZTA substrates contain < 30 mol% ZrO_2.[13–15]

TABLE 3 Compositions of ZTA films

Composition	ZrO_2 content	Dopants, wt%
A	30 mol%	—
B	30 mol%	1 wt% TiO_2 CP[a]
C	30 mol%	1 wt% TiO_2 NP[b]
D[c]	10 mol%	1 wt% TiO_2 NP, 1 wt% MgO

[a]CP: commercial powder from Evonik Industries AG, Germany. APS ≈ 20 nm but may be agglomerated.

[b]NP: nanopowder by LF-FSP, APS = 20-30 nm.

[c]A mixture of LF-FSP-produced 30 mol.% ZrO_2-doped Al_2O_3, 2 wt.% MgO-doped Al_2O_3,[10] and 1 wt% TiO_2 NP.

Figure 4 compares the SEM fracture surfaces of films **A**-**D** (Table 3) sintered at 1300°C-1500°C/5 h/O_2 (**Figure S1A**). At 1300°C, all films are not dense, but the grains of 30 mol% ZrO_2-doped Al_2O_3 supplemented with TiO_2 (**B** and **C**) show significant grain growth compared to films without TiO_2 (**A**) as expected.[7,8,37–40] In contrast, the Al_2O_3 film doped with 10 mol% ZrO_2, 1 wt% TiO_2 NP, and MgO (**D**) shows small AGSs which are comparable to film **A**, a result of MgO doping that prevents excessive grain growth.[10,40–51]

At 1400°C, 30 mol% ZrO_2-doped Al_2O_3 films supplemented with TiO_2 (**B** and **C**) are already dense with intergranular fracture surfaces. The Al_2O_3 film with 10 mol% ZrO_2 (**D**) starts to densify. At 1450°C, films **B** and **C** show abnormal grain growth; the 30 mol% ZrO_2-doped Al_2O_3 without TiO_2 (**A**) starts to densify with uniform grain sizes.

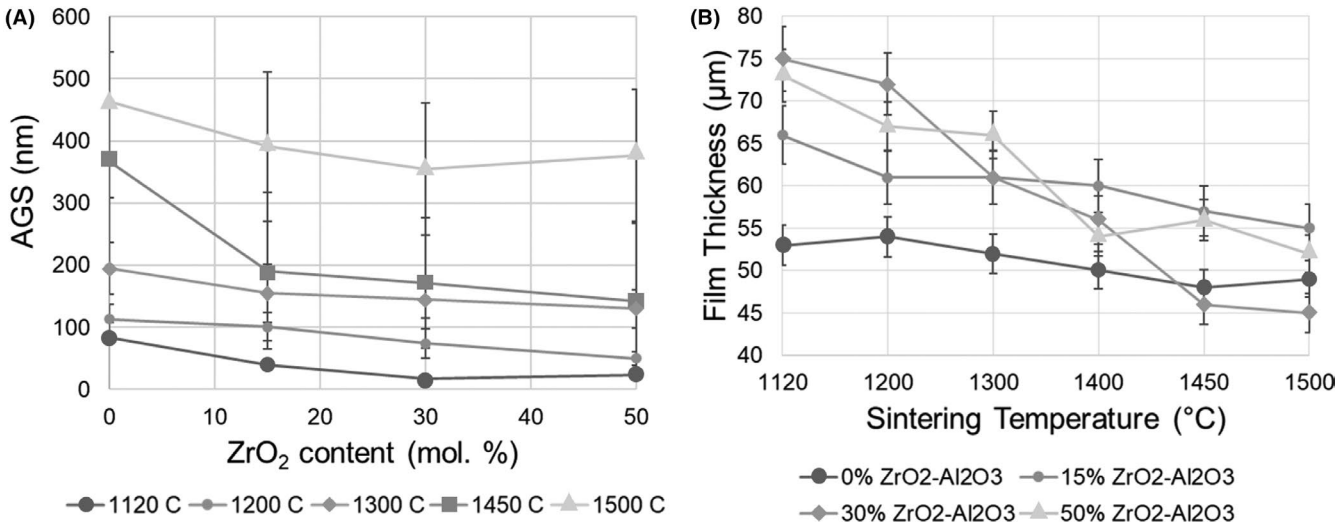

FIGURE 3 A, AGSs vs ZrO_2 content B, sintered film thicknesses for $(ZrO_2)_x(Al_2O_3)_{1-x}$ (x = 0, 15, 30, and 50 mol%)

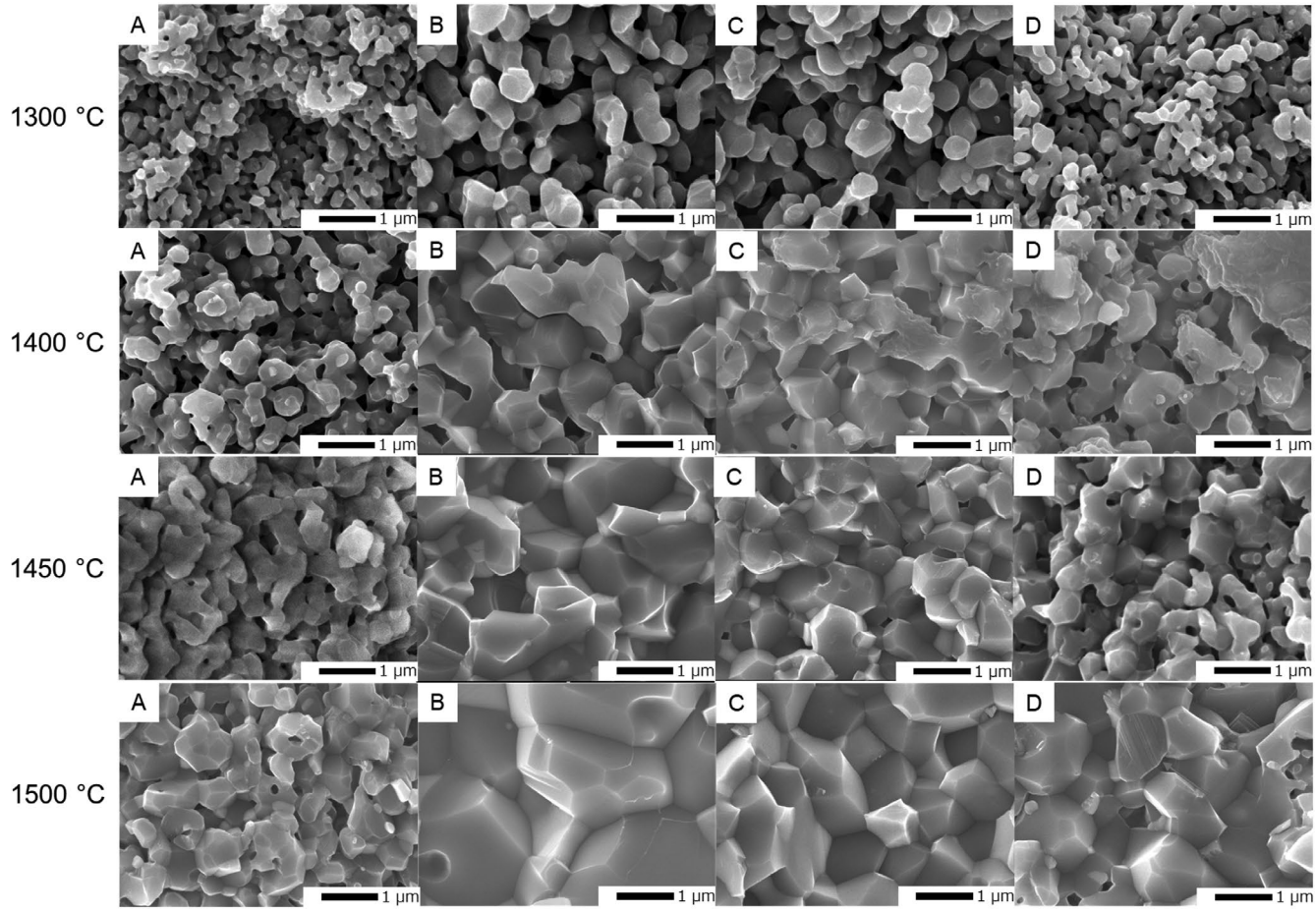

FIGURE 4 SEM fracture surfaces of ZTA films (A-D, per Table 3) sintered at 1300°C-1500°C/5 h/O_2. The arrow suggests transgranular fracture

These films show significant differences in AGSs when sintered at 1500°C per Figure 4 bottom. Film **A** shows a rather small AGSs of ≈200 nm with visible pores. Excess grain growth is exhibited in film **B** (AGSs ≈ 1-2 μm). Films **C** and **D** show similar AGSs of ≈500 nm. Film **D** exhibits some transgranular (intra-) fracture behavior (marked with arrow) suggesting improved mechanical properties at grain boundaries.

Figure 5 presents the XRDs of the films sintered at 1300°C-1500°C/5 h/O_2. The films consist mainly of α-Al_2O_3 (corundum, hexagonal, space group 167, PDF-98-001-1217) and *t*-ZrO_2 (tetragonal, space group 137, PDF-04-013-6616); some films show small peaks at 36°, 40°, 48°, and 49° 2θ (not marked in Figure 5) corresponding to a calcite phase (hexagonal, space group 167), which is likely a result of residual carbon from insufficient O_2 during LF-FSP. Overall, no *m*-ZrO_2 is observed; similar phases are exhibited for films with different compositions and sintering conditions.

A similar sintering study on the films **A**-**D** was repeated in N_2/H_2 (see Figure S1B schedule). Since the films barely sinter at 1300°C/5 h/O_2 (Figure 4), a similar outcome in N_2/H_2 is expected and therefore only sintering at 1400°C-1500°C/5 h/N_2/H_2 was explored.

Figure 6 compares SEM fracture surfaces of films **A**-**D** sintered at 1400°C-1500°C/5 h/N_2/H_2. Similar densification behaviors are observed as in O_2. Films **B** and **C** start to densify at 1400°C, and obvious grain growth can be seen at 1500°C, especially for film **B**. Films **A** and **D** show similar sintering behavior, they densify at 1500°C, and exhibit finer grain sizes (~0.5-1 μm) than **B** and **C** (≥ 1 μm). As discussed, TiO_2 promotes grain growth and densification,[7,8,37–40] while MgO tends to diffuse to the grain boundaries and limits grain growth.[10,40–51]

After sintering at 1500°C, all films show some transgranular fracture behavior (marked with arrows), suggesting improved mechanical properties.

Film lateral shrinkage was measured before and after sintering per Table 4. Overall, shrinkage increases with sintering temperature. At 1500°C in both O_2 and N_2/H_2, films with different compositions show similar lateral shrinkages of ~20%. Films with composition **B** have the highest lateral shrinkage, recall that they have much larger AGSs (1-2 μm at 1500°C/O_2 and N_2/H_2), as seen in Figures 4 and 6. This suggests, as expected, that TiO_2 CP promotes densification and grain growth, resulting in higher shrinkages and larger AGSs.

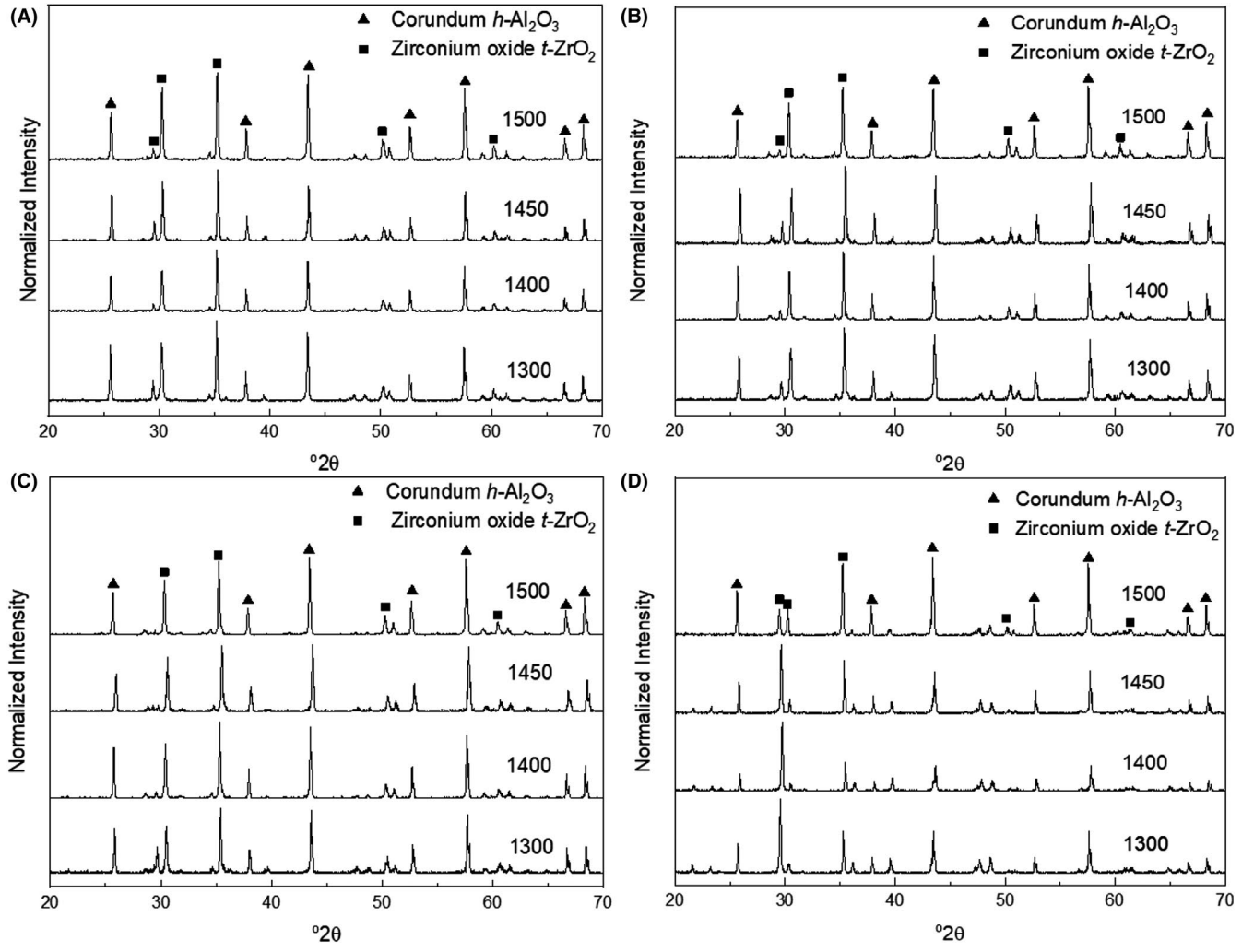

FIGURE 5 XRDs of ZTA films (A-D, per Table 3) sintered at 1300°C-1500°C/5 h/O_2

TiO_2 LF-FSP NPs also promote densification (Figures 4 and 6), and film **C** starts to densify at 1400°C, but smaller AGSs result compared to film **B**, likely a result of the smaller APSs of TiO_2 LF-FSP NPs compared to TiO_2 CP. Film **D** with both TiO_2 and MgO doping generally shows both smaller and more uniform AGSs compared to film **C** under different sintering conditions (Figures 4 and 6).

Figure S5 shows XRDs of the films sintered at 1400°C-1500°C/5 h/N_2/H_2. Similar to films sintered in O_2, they mainly contain α-Al_2O_3 and *t*-ZrO_2; the impurity calcite phase (36°, 40°, 48°, and 49° 2θ) is also observed in some films. Phase compositions of the different films are also very similar, and no *m*-ZrO_2 is observed. The composition does not change with different sintering conditions.

The conclusions from the thin film work are that films with composition **D** per Table 3 show small and uniform grain sizes (0.5-1 μm), and low porosity. They are almost fully dense when sintered at 1500°C/5 h, in either O_2 or N_2/H_2 per SEM observations (Figures 4 and 6). These results were then extended to processing ~200 μm thick ZTA films with the same composition.

5 | ZTA ~200 μm thick films

In this section, the sinterability, microstructures, and fractural toughness of ZTA films up to ~200 μm thick and ~ 2×2 cm^2 were investigated for possible application as power electronic substrates[11–14] using composition **D** from the above studies.

We first started by targeting ~ 200 μm thick ZTA films with small sizes (~1 × 1 cm^2) sintered at 1500°C/5 h in O_2 or N_2/H_2 to compare sintering behavior in different atmospheres. Figure 7 compares SEM fracture surfaces of ZTA films (composition **D**) sintered at 1500°C/5 h in O_2 and N_2/H_2. Films sintered in different atmospheres show similar morphologies with AGSs of 0.5-1 μm. Films sintered in N_2/H_2 show slightly smaller AGSs, greater shrinkage in both lateral and vertical dimensions (Figure 7 and Table 5), and lower porosity (Figure 7D vs. **7c**), suggesting that N_2/H_2 provides higher densities, in agreement with previous work on MgO (0-5 wt%)-doped Al_2O_3 thin films.[10]

Figure S6 shows XRDs of ZTA films (composition D) sintered in O_2 and N_2/H_2, respectively. Similar to thin films above, both films exhibit two main phases: α-Al_2O_3

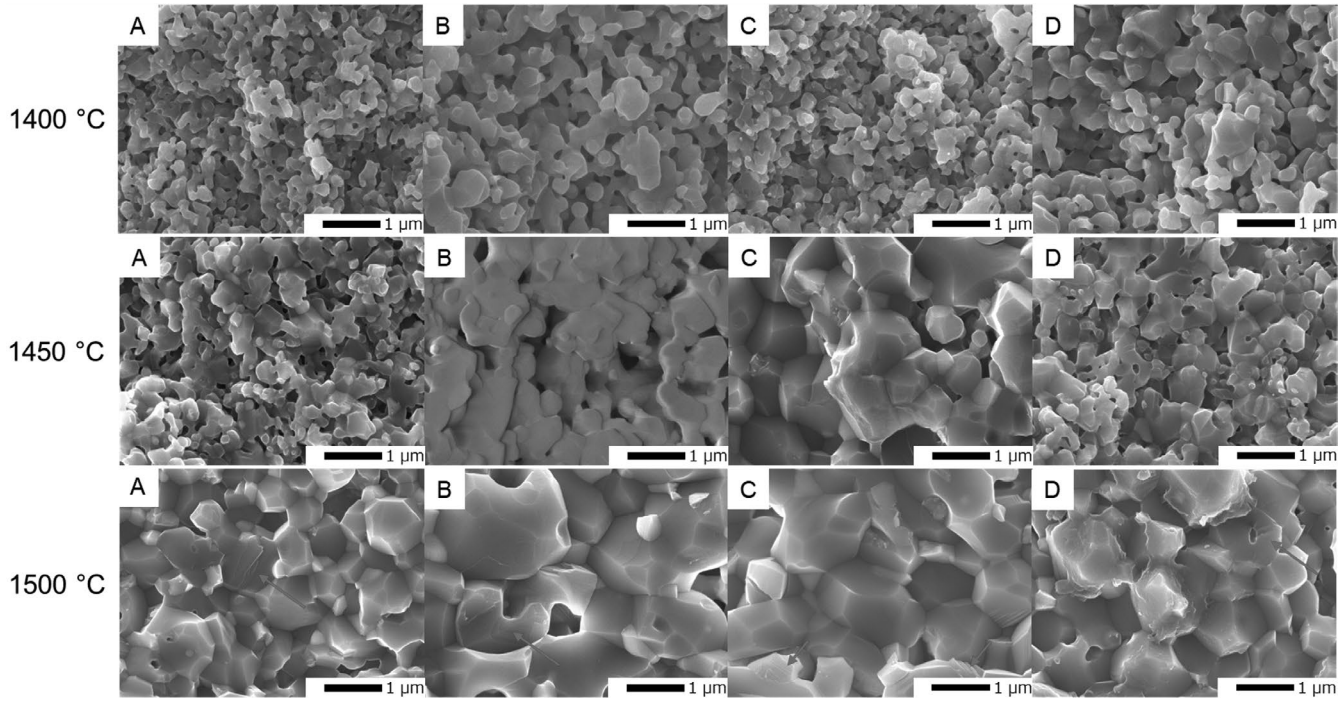

FIGURE 6 SEM fracture surfaces of ZTA films (A-D, per Table 3) sintered at 1400°C-1500°C/5 h/N2/H2. Arrows suggest transgranular fracture

TABLE 4 Lateral shrinkage of ZTA films (A-D per Table 3) sintered at 1400°C-1500°C/5 h/N_2/H_2

	Lateral shrinkage, %			
Sintering condition	**A**	**B**	**C**	**D**
1400°C/5 h/N_2/H_2	14	10	14	12
1450°C/5 h/N_2/H_2	16	19	22	18
1500°C/5 h/N_2/H_2	24	25	24	22
1500°C/5 h/O_2	19	25	22	22

(hexagonal) and *t*-ZrO_2, but the impurity phase (calcite) disappears. No obvious difference in phase compositions is observed for films sintered in different atmospheres.

Studies on smaller (~1 × 1 cm^2), ~200 μm ZTA films suggested that N_2/H_2 sintering provides higher densities. Therefore, we continued studies on larger films (~2 × 2 cm^2) sintered in N_2/H_2. Initially, the same sintering schedule with a ramp rate of 5°C/min was used (Figure S1B). However, as seen in Figure S7, the larger films cracked while smaller films remained intact after sintering.

It is likely that the fast ramp rate leads to fast shrinkage and cracking. Therefore, the ramp rate was reduced to 2.5 and then 1°C/min while following the same schedule per Figure S1B, but the larger films still cracked (Figure S7). Only one large film out of three sintered at 1°C/min was crack-free. This suggests that a slow ramp rate will prevent cracking, but it is a very inefficient method (long sintering time:> 24 h) that provides small improvements.

In addition, these films bonded to the Al_2O_3 substrates after sintering, a likely source of stress that results in cracking. Therefore, an insulating boron nitride (BN) powder layer was introduced as it is stable to ~2000°C, see below.

SEMs of ~200 μm ZTA films sintered at different ramp rates show small differences (Figure 8). All films were dense with similar AGSs of 1-2 μm. However, films sintered at lower ramp rates (2.5 and 1°C/min) show slightly larger grains (Figure 8 and Table 6), likely due to the longer sintering times. The sintered thicknesses varied between 175 and 210 μm. Table 6 summarizes AGSs, shrinkage, and density changes on sintering.

Generally, slower ramp rates caused greater shrinkages and higher densities, but overall densities (~90%) are low while AGSs increased compared to small films per Figure 7 and Table 5, likely due to undesired adherence of the ZTA films to the Al_2O_3 substrates inhibiting shrinkage and therefore densification, while coincidentally generating larger AGSs.

Figure S8 compares XRDs of ~200 μm ZTA films sintered at different ramp rates. No obvious differences can be seen; all the films show two main phases without impurities: α-Al_2O_3 and *t*-ZrO_2.

To eliminate cracking, an insulating BN layer (powder from Sigma-Aldrich) was introduced to prevent bonding with the Al_2O_3 substrates. Additionally, sintering following different binder burnout temperatures of 600°C, 800°C, and 1100°C was investigated. The binder burnout atmosphere was changed from O_2 to air, reducing the rate of

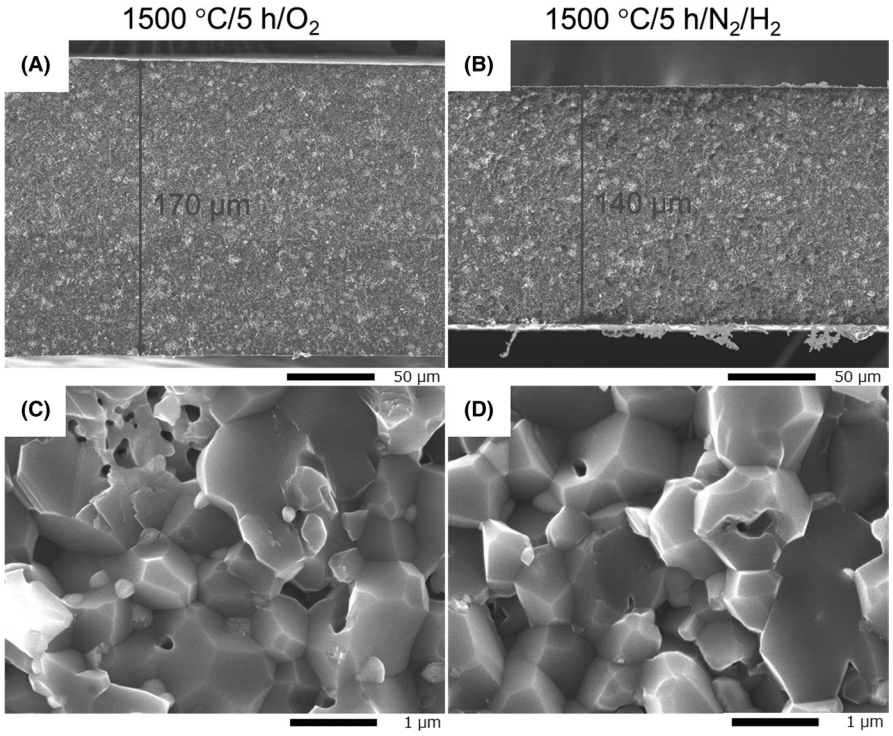

FIGURE 7 SEM fracture surfaces of ZTA films (composition D, size ≈ 1 × 1 cm^2 × 200 µm) sintered at 1500°C/5 h/O2 (A, C), and 1500°C/5 h/ N2/ H2 (B, D). Initial thickness ≈ 200 µm before sintering

TABLE 5 AGSs and shrinkages of ZTA films (composition D, size ≈1 × 1 cm^2 × 200 µm)

Sintering condition	AGS, µm	Lateral shrinkage, %	Vertical shrinkage, %
1500°C/5 h/O_2	0.9 ± 0.2	19	17
1500°C/5 h/N_2/H_2	0.8 ± 0.2	22	24

oxidative decomposition. The sintering schedule is provided in Figure S9.

Figure S10 compares films sintered at different binder burnout temperatures with BN interfaces. Films debindered at 800°C/1 h/air stayed mostly intact after sintering. However, films debindered at 600°C/1 h/air formed large cracks, and films debindered at 1100°C/1 h/air cracked into pieces. Such differences in film quality suggest that cracking is primarily related to binder burnout.

Figure S11 compares SEMs of ~200 µm ZTA films with different binder burnout temperatures with BN insulation. Films debindered at 600°C/1 h/air show the lowest porosities and smallest AGSs of 0.7 µm among the three (Table 7). All films show similar vertical shrinkages of ~20% (Table 7). Figure S12 compares XRDs of 200 µm ZTA films with different binder burnout temperatures. As with the above XRD studies, no obvious differences are observed; all films show two main phases of α-Al_2O_3 and *t*-ZrO_2 without impurity.

To further investigate the binder burnout mechanism, a TGA-DTA was run on the 10 mol% ZrO_2-doped Al_2O_3 green films (composition D, Figure S13). A decomposition exotherm for the organics appears between ~180°C and 500°C. Accordingly, the sintering schedule was modified per Figure S14 with a three-step binder burnout procedure: first holding at 200°C/1 h and slowly (1°C/min) ramping up to 500°C, then ramping up (2.5°C/min) to 800°C/1 h.

Figure 9 shows optical images of ~200 µm ZTA films before and after sintering. After binder burnout, all films only show minimal size changes. Shrinkage and coincident densification occur primarily during sintering. Films with thicknesses ≤ 200 µm after sintering are crack-free, while films with thicknesses >220 µm exhibit small cracks. All films remain mostly intact with better quality compared to the above films (Figures S7 and S10).

As shown in Figure 10, films sintered using the three-step binder burnout procedure show low porosities and small AGSs of 0.7 µm after sintering. Table 7 compares AGSs, shrinkages, and densities of ZTA films sintered using different binder burnout conditions with BN insulation. All films have densities of 97%–99% determined by Archimedes method, which improve significantly from films sintered without BN insulation (~90% dense, Table 6). In addition, the AGSs of films sintered with BN decreased (≤1 µm) compared to films without (1.3-1.6 µm, Table 6). The use of BN powder between ZTA films and Al_2O_3 improves film densities and reduces AGSs, as the substrate effects are eliminated.

Fracture toughness (K_{1C}) measurements were undertaken using a single-edge precracked beam test (SEPB) on the ~200 µm ZTA films (composition D) sintered with a three-step binder burnout procedure (Figure S14) as they show optimum qualities compared to other films. As given in

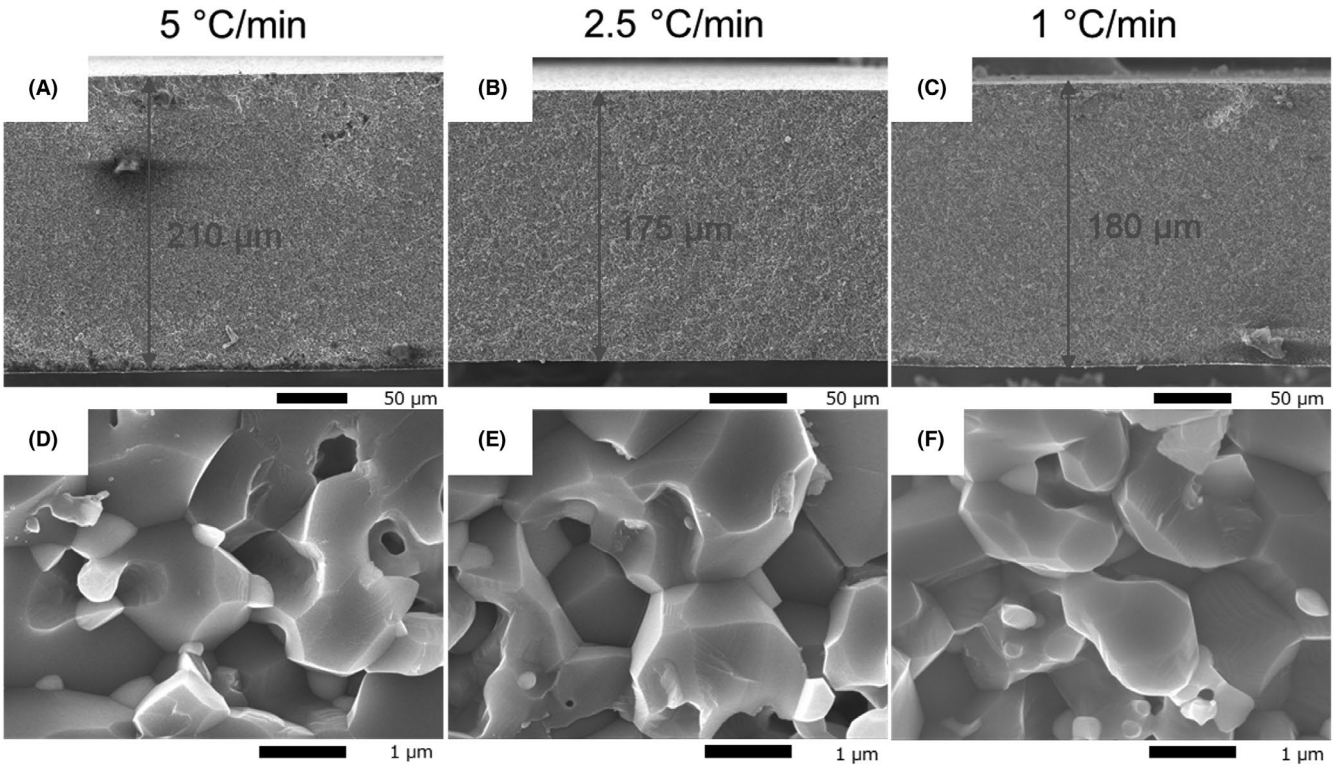

FIGURE 8 SEM fracture surfaces of ~200 µm ZTA films (composition D) sintered (1500°C/5 h/N2/H2) at 5°C/min (A, D), 2.5°C/min (B, E), and 1°C/min (C, F). Green film thicknesses were 220-250 µm before sintering

TABLE 6 Selected properties of ~200 µm ZTA films (composition D) sintered at 1500°C/5 h/N_2/H_2 with different sintering ramp rates

Ramp rate, °C/min	AGS, µm	Lateral shrinkage, %	Vertical shrinkage, %	Measured density[a], g/cm^3	Theoretical density[a], g/cm^3	Relative density, %
5	1.3 ± 0.3	20	16	3.62	4.04	89.7
2.5	1.5 ± 0.3	22	24	3.66	4.03	90.7
1	1.6 ± 0.4	23	23	3.68	4.04	91.2

[a]Film densities are measured by the Archimedes method; theoretical densities are calculated from phase compositions analyzed by XRD refinement.

TABLE 7 Selected properties of ~200 µm ZTA films (composition D) sintered at different binder burnout conditions with BN insulation

Binder burnout condition	AGS, µm	Lateral shrinkage, %	Vertical shrinkage, %	Measured density, g/cm^3	Theoretical density, g/cm^3	Relative density, %
600°C/1 h/air	0.7 ± 0.1	20	20	4.05	4.10	98.8
800°C/1 h/air	0.8 ± 0.1	21	21	4.07	4.12	98.8
1100°C/1 h/air	1.1 ± 0.1	N/A[a]	21	4.00	4.12	97.1
3-step burnout	0.7 ± 0.1	17	19	4.02	4.10	98.1

[a]Films debindered at 1100°C/1h/air cracked into pieces and failed to give accurate lateral lengths after sintering.

Figure S15, ~200 µm 10 mol% ZrO_2-doped Al_2O_3 films show K_{1C} values in a range of 15-38 MPa m$^{1/2}$ (three samples) with an average of 24 MPa m$^{1/2}$, which is two to four times higher than the reported values. Such a high K_{1C} value may be attributed to the fine and uniform ceramic microstructures sintered from NPs by LF-FSP, retained *t*-ZrO_2 phase after sintering, TiO_2 and MgO doping, and improved film qualities through sintering refinement.

6 | COATING Si_3N_4 SUBSTRATES WITH ZTA THIN FILMS

In this section, above results provide the basis for formulating and processing thin ZTA films (composition **D** per Table 3) on ~300 µm Si_3N_4 films as a bonded physical layer to minimize oxidation for high-temperature substrates and power electronic applications. As discussed in the previous section, ZTA

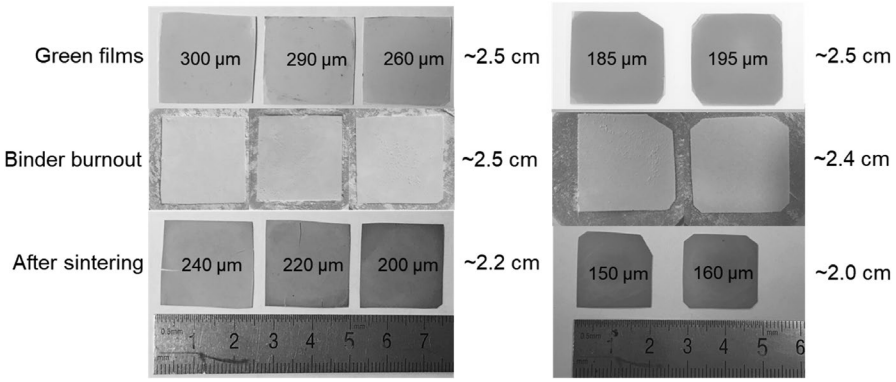

FIGURE 9 Optical images of ~200 µm ZTA films (composition D) before and after binder burnout and sintering (see schedule in Figure S14). Thicknesses are given on the films, and lateral lengths are given on the right

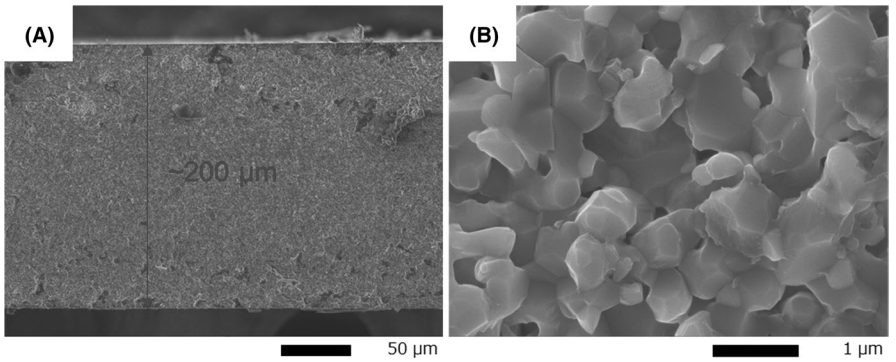

FIGURE 10 SEM fracture surfaces of ~200 µm ZTA film (composition D) sintered with three-step binder burnout procedure per Figure S14

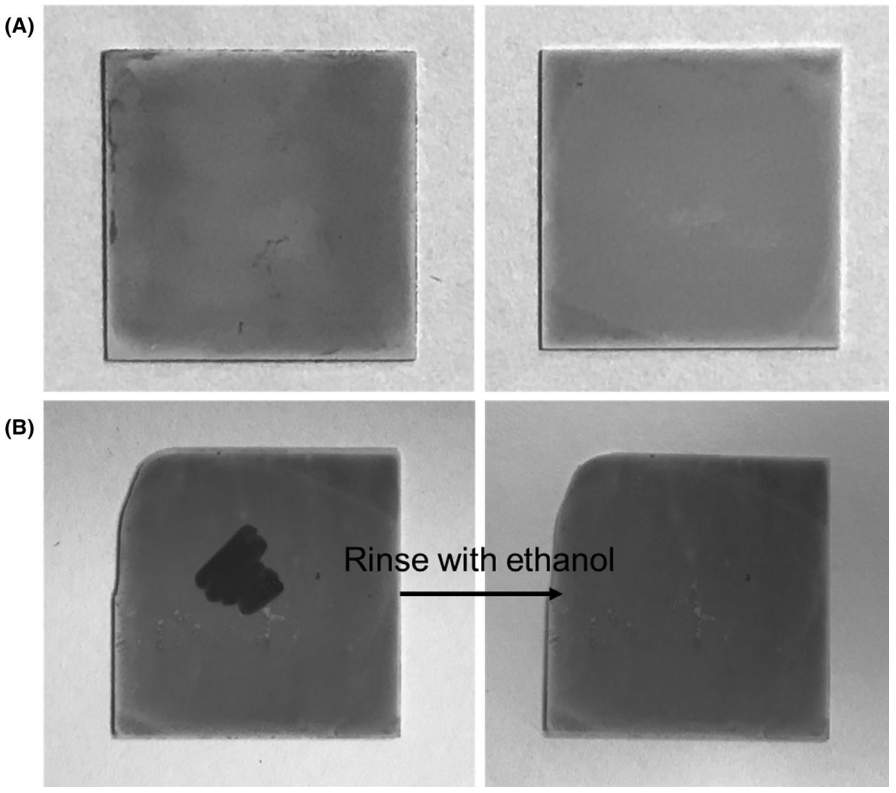

FIGURE 11 Representative examples A, and dye test B, of Si_3N_4 films coated with ZTA (composition D) after sintering at 1500°C/5 h/N2/H2

films with composition **D** show a high K_{1C} and density, therefore we continued coating studies with the same composition.

Figure 11A shows surfaces of coated Si_3N_4 films sintered at 1500°C/5 h/N_2/H_2. Compared to uncoated films in Figure S2, the coating appears to be light grey and uniform. As shown in Figure 11B, A coated Si_3N_4 film was marked with red dye and then rinsed with ethanol. After rinsing, the mark disappears completely, which

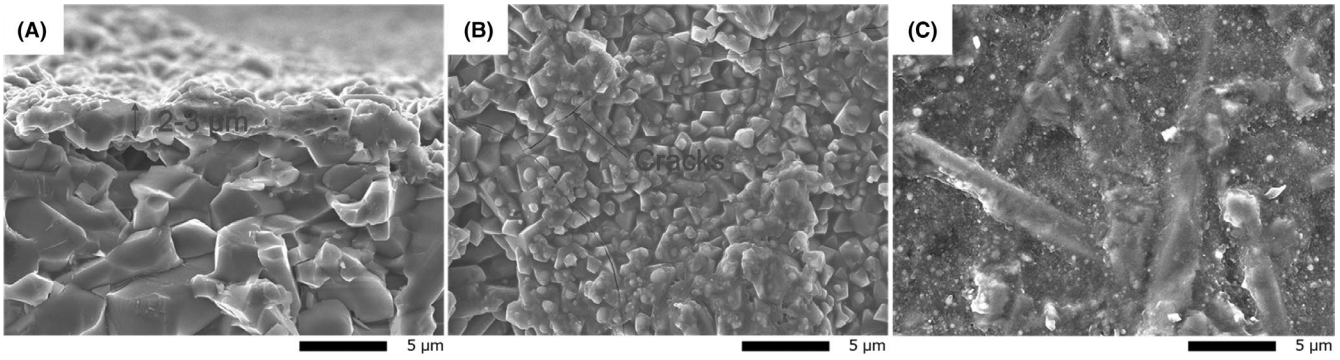

FIGURE 12 SEM fracture surface A, and surface B, of Si3N4 films coated with ZTA (composition D) sintered at 1500°C/5 h/N2/H2. C, SEM surface of an uncoated Si3N4 film

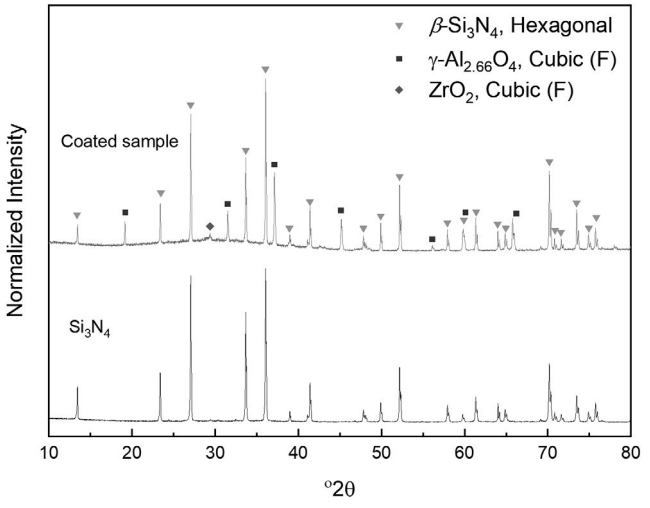

FIGURE 13 XRDs of Si_3N_4 films coated with ZTA (composition D) sintered at 1500°C/5 h/N2/H2

suggests that the die does not penetrate through unseen cracks and that the coating is stable, smooth, and crack-free.

Figure 12 and S16 show SEMs and EDSs of coated Si_3N_4 films. For coated films, the rod-like Si_3N_4 structure at the surface (Figure 12C) is replaced by a dense, homogeneous Al-rich coating with finer grains (Figure 12B and S16). The fracture surface suggests the coating is 2-3 μm thick (Figure 12A). However, there are small cracks propagating along the surface (Figure 12B), which may be introduced by thermal pressing or the sample breaking during SEM preparation, which requires small sample sizes ($\leq 0.5 \times 0.5$ cm^2).

As shown in Figure 13 XRDs, coated Si_3N_4 films present hexagonal β-Si_3N_4, as found in the original Si_3N_4 film. A cubic γ-$Al_{2.66}O_4$ phase appears with a trace of cubic ZrO_2, indicating that the 10 mol% ZrO_2-doped Al_2O_3 likely reacts or partially reacts with the Si_3N_4 substrate resulting in a structural distortion again suggesting good bonding.

Uncoated and coated Si_3N_4 films were heated to 1500°C/1 h/O_2 to assess resistance to oxidation. As shown in Figure 14, the uncoated Si_3N_4 film suffers more damage than the coated sample. The edges of both films show more visible damage than the centers. During heating, films were sandwiched between Al_2O_3 substrates; the edges were more

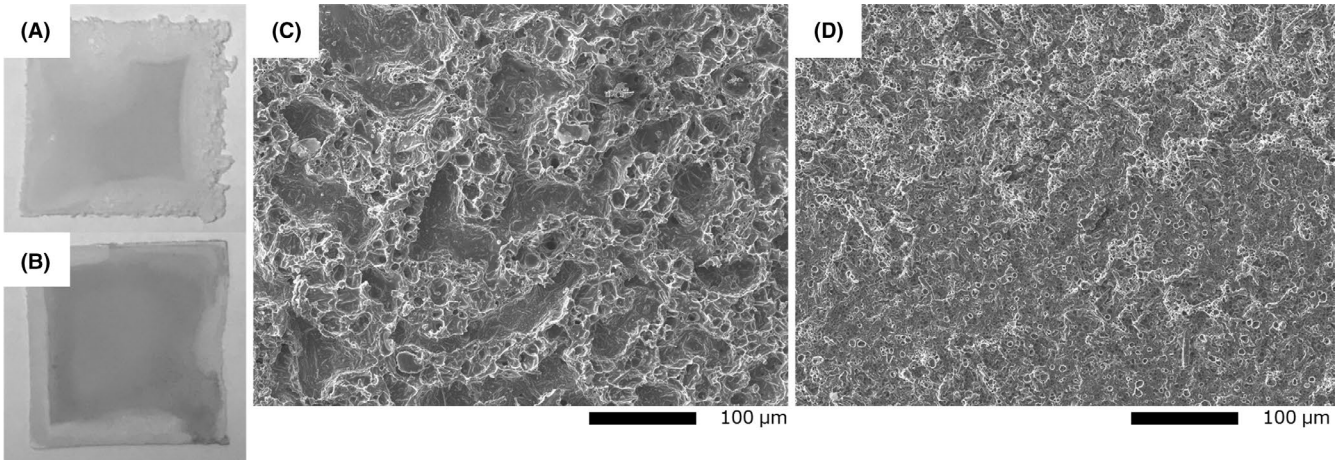

FIGURE 14 Optical images of A, uncoated and B, coated Si_3N_4 films and SEM surfaces of C, uncoated and D, coated Si_3N_4 films with ZTA (composition D) after heating at 1500°C/1 h/O_2

exposed to O_2 than the center. SEM surface images of the uncoated Si_3N_4 film reveal large cavities from obvious oxidation, while the coated film exhibits a smoother microstructure (Figure 14C,D). Overall, it is evident that the coating protects Si_3N_4 films against oxidization, even under extreme conditions.

7 | CONCLUSIONS

In summary, we investigated the sinterability, microstructures, and phase compositions of ZTA thin films (~40 μm) with varying compositions and sintering conditions starting from $(ZrO_2)_x(Al_2O_3)_{1-x}$ (x = 0-50 mol%) NPs by LF-FSP. Studies suggest that 1 wt% MgO and TiO_2 additives improve the sintering behavior, resulting in dense films (composition **D**: 10 mol% ZrO_2-doped Al_2O_3 with 1 wt% TiO_2 and MgO) with final AGSs of 0.5-1 μm at 1500°C. Comparison of films sintered in O_2 and N_2/H_2 suggests that the N_2/H_2 atmosphere improves film quality coincident with higher shrinkages and densities, and smaller reductions in AGSs.

For potential applications as power electronic substrates, ZTA film thicknesses were increased to 150-250 μm. Sintered films exhibit hexagonal α-Al_2O_3 and t-ZrO_2 phases, which in principle provide good mechanical properties, and was proved by SEPB test that a high K_{1C} value of ~24 MPa $m^{1/2}$ is obtained. By investigating the effects of different sintering conditions, we were able to sinter crack-free 150-250 μm thick 10 mol% ZrO_2-doped Al_2O_3 films with AGSs of 0.7 μm by using BN insulation between films and Al_2O_3 substrates with a three-step binder burnout procedure.

Finally, ZTA thin films (composition **D**) form homogenous coatings on Si_3N_4 substrates with thicknesses < 5 μm that offer protection under extreme oxidative conditions (1500°C/1 h/O_2), suggesting an alternate application of ZTA films for high-temperature ceramics and power electronic substrates.

ACKNOWLEDGMENT

We are grateful for the support of this work by Rogers Corp., as well as their provided Si_3N_4 substrates and fracture toughness SEPB test on ZTA films. We also thank Makoto Takeuchi for his effort on MgO-doped (0-5 wt%) Al_2O_3 thin films (<10 μm)[10] that provided motivation and help on the present work.

ORCID

Xinyu Zhang https://orcid.org/0000-0003-2971-9185
Richard M. Laine https://orcid.org/0000-0003-4939-3514

REFERENCES

1. Dorre E, Hubner H. Alumina: processing, properties and applications. Berlin Heidelberg: Springer-Verlag; 1984.
2. Rao PK, Jana P, Ahmad MI, Roy PK. Synthesis and characterization of zirconia toughened alumina ceramics prepared by co-precipitation method. Ceram Int. 2019;45(13):16054–61.
3. Isfahani T, Javadpour J, Khavandi A. Formation mechanism and phase transformations in mechanochemically prepared Al_2O_3-40wt% ZrO_2 nanocomposite powder. Compos Interfaces. 2019;26(10):887–904.
4. Sarkar D, Mohapatra D, Ray S, Bhattacharyya S, Adak S, Mitra N. Synthesis and characterization of sol-gel derived ZrO_2 doped Al_2O_3 nanopowder. Ceram Int. 2007;33(7):1275–82.
5. Sarkar D, Adak S, Mitra NK. Preparation and characterization of an Al_2O_3-ZrO_2 nanocomposite, part I: powder synthesis and transformation behavior during fracture. Compos Part Appl Sci Manuf. 2007;38(1):124–31.
6. Ganesh I, Olhero SM, Torres PMC, Alves FJ, Ferreira JMF. Hydrolysis-induced aqueous gelcasting for near-net shape forming of ZTA ceramic composites. J Eur Ceram Soc. 2009;29(8):1393–401.
7. Zu Y, Chen G, Fu X, Luo K, Wang C, Song S, et al. Effects of liquid phases on densification of TiO_2-doped Al_2O_3-ZrO_2 composite ceramics. Ceram Int. 2014;40(3):3989–93.
8. Chen G, Zu Y, Luo J, Fu X, Zhou W. Microstructure and superplastic behavior of TiO_2-doped Al_2O_3-ZrO_2 (3Y) composite ceramics. Mater Sci Eng A. 2012;554:6–11.
9. Yu W, Zheng Y, Yu Y, Su X. Microstructural evolution of supra-nanostructure Al_2O_3/ZrO_2 eutectic powders by combustion synthesis-spray cooling. J Am Ceram Soc. 2019;102(12):7689–98.
10. Takeuchi M, Niedermaier M, Jansohn M, Umehara N, Laine RM. Processing thin (<10μm), dense, flexible α-Al_2O_3 films from nanopowders. J Ceram Soc Jpn. 2019;127(2):81–9.
11. Gundel P, Persons R, Bawohl M, Challingsworth M, Czwickla C, Garcia V, et al. Highly reliable and cost effective thick film substrates for power LEDs. In: 2016 IEEE Applied Power Electronics Conference and Exposition (APEC) [Internet]. Long Beach, CA: IEEE; 2016. p. 3069–74. https://doi.org/10.1109/APEC.2016.7468301
12. Maeder T, Jacq C, Ryser P. Long-term mechanical reliability of ceramic thick-film circuits and mechanical sensors under static load. Sens Actuators Phys. 2012;186:210–8.
13. Srikanth C, Madhu GM. Effect of ZTA concentration on structural, thermal, mechanical and dielectric behavior of novel ZTA–PVA nanocomposite films. SN Appl Sci. 2020;2(3):422.
14. Mussavi Rizi SH, Ghatee M. A study of mechanical properties of alumina–zirconia composite films prepared by a combination of tape casting and solution impregnation method. J Aust Ceram Soc. 2020;56(1):167–74.
15. Miric A, Dietrich P. Inorganic substrates for power electronics applications. Heraeus Dtschl. 2013;1–7.
16. Chen I-W, Xue LA. Development of superplastic structural ceramics. J Am Ceram Soc. 1990;73(9):2585–609.
17. Wang X, Padture NP, Tanaka H. Contact-damage-resistant ceramic/single-wall carbon nanotubes and ceramic/graphite composites. Nat Mater. 2004;3(8):539–44.
18. Chen P, Chen J, Guo B, Liu H. Measurement of the dynamic fracture toughness of alumina ceramic. In: Song B, Lamberson L, Casem D, Kimberley J, editors. Dynamic behavior of materials, volume 1 [Internet] (Conference Proceedings of the Society for Experimental Mechanics Series). Cham: Springer International Publishing; 2016: 33–8.

19. Casellas D, Nagl MM, Llanes L, Anglada M. Fracture toughness of alumina and ZTA ceramics: microstructural coarsening effects. J Mater Process Technol. 2003;144:148–52.
20. Green DJ. Critical microstructures for microcracking in Al_2O_3-ZrO_2 composites. J Am Ceram Soc. 1982;65(12):610–4.
21. Tuan WH, Chen RZ, Wang TC, Cheng CH, Kuo PS. Mechanical properties of Al_2O_3/ZrO_2 composites. J Eur Ceram Soc. 2002;22(16):2827–33.
22. Dresvyannikov AF, Petrova EV, Khairullina AI. Electrochemical synthesis and physicochemical properties of nanostructured Al_2O_3–ZrO_2–MgO oxide systems. Prot Met Phys Chem Surf. 2020;56(1):89–93.
23. Abi CB, Emrullahoğlu OF, Said G. Microstructure and mechanical properties of MgO-stabilized ZrO_2-Al_2O_3 dental composites. J Mech Behav Biomed Mater. 2013;18:123–31.
24. Gao L, Liu Q, Hong JS, Miyamoto H, De La Torre SD, Kakitsuji A, et al. Phase transformation in the Al_2O_3-ZrO_2 system. J Mater Sci. 1998;33(6):1399–403.
25. Wakai F, Iga T, Nagano T. Effect of dispersion of ZrO_2 particles on creep of fine-grained Al_2O_3. J Ceram Soc Jpn. 1988;12:1206–9.
26. Yoshida H, Okada K, Ikuhara Y, Sakuma T. Improvement of high-temperature creep resistance in fine-grained Al_2O_3 by Zr^{4+} segregation in grain boundaries. Philos Mag Lett. 1997;76(1):9–14.
27. Kim M, Laine RM. Liquid-feed flame spray pyrolysis (LF-FSP) for combinatorial processing of nanooxide powders along the $(ZrO_2)_{1-x}(Al_2O_3)_x$ tie-line. Phase segregation and the formation of core-shell nanoparticles. J Ceram Process Res. 2007;8(2):129–36.
28. Kim M, Laine RM. Pressureless sintering t-zirconia@δ-Al_2O_3 (54 mol%) core-shell nanopowders at 1120°C provides dense t-zirconia-toughened α-Al_2O_3 nanocomposites. J Am Ceram Soc. 2010;93(3):709–15.
29. Kim M. Mixed-metal oxide nanopowders by liquid-feed flame spray pyrolysis (LF-FSP): synthesis and processing of core-shell nanoparticles [Thesis]. Ann Arbor (MI): University of Michigan; 2008.
30. Zhao Z, Zhang L, Song Y, Wang W, Wu J. Microstructures and properties of rapidly solidified Y_2O_3 doped Al_2O_3/ZrO_2 composites prepared by combustion synthesis. Scr Mater. 2006;55(9):819–22.
31. Pena JI, Merino RI, Harlan NR, Larrea A, De la Fuente GF, Orera VM. Microstructure of Y_2O_3 doped Al_2O_3-ZrO_2 eutectics grown by the laser floating zone method. J Eur Ceram Soc. 2002;22(14–15):2595–602.
32. Lee JH, Yoshikawa A, Kaiden H, Lebbou K, Fukuda T, Yoon DH, et al. Microstructure of Y_2O_3 doped Al_2O_3/ZrO_2 eutectic fibers grown by the micro-pulling-down method. J Cryst Growth. 2001;231(1–2):179–85.
33. Yoshida H, Kuwabara A, Yamamoto T, Ikuhara Y, Sakuma T. High temperature plastic flow and grain boundary chemistry in oxide ceramics. J Mater Sci. 2005;40(12):3129–35.
34. Yi E, Wang W, Mohanty S, Kieffer J, Tamaki R, Laine RM. Materials that can replace liquid electrolytes in Li batteries: Superionic conductivities in $Li_{1.7}Al_{0.3}Ti_{1.7}Si_{0.4}P_{2.6}O_{12}$. Processing combustion synthesized nanopowders to free standing thin films. J Power Sources. 2014;269(10):577–88.
35. Yi E, Wang W, Kieffer J, Laine RM. Flame made nanoparticles permit processing of dense, flexible, Li^+ conducting ceramic electrolyte thin films of cubic-$Li_7La_3Zr_2O_{12}$ (c-LLZO). J Mater Chem A. 2016;4(33):12947–54.
36. Yi E, Temeche E, Laine RM. Superionically conducting β′′-Al_2O_3 thin films processed using flame synthesized nanopowders. J Mater Chem A. 2018;6:12411–9.
37. Wang CJ, Huang CY. Effect of TiO_2 addition on the sintering behavior, hardness and fracture toughness of an ultrafine alumina. Mater Sci Eng A. 2008;492(1–2):306–10.
38. Bagley RD, Cutler IB, Johnson DL. Effect of TiO_2 on initial sintering of Al_2O_3. J Am Ceram Soc. 1970;53(3):136–41.
39. Brook RJ. Effect of TiO_2 on initial sintering of Al_2O_3. J Am Ceram Soc. 1972;55(2):114.
40. Roy SK, Coble RL. Solubilities of magnesia, titania, and magnesium titanate in aluminum oxide. J Am Ceram Soc. 1968;51(1):1–6.
41. Kosmac T, Wallace JS, Claussen N. Influence of MgO additions on the microstructure and mechanical properties of Al_2O_3-ZrO_2 composites. J Am Ceram Soc. 1982;65(5):c66–67.
42. Coble RL. Sintering crystalline solids. II. Experimental test of diffusion models in powder compacts. J Appl Phys. 1961;32(5):793–9.
43. Bennison SJ, Harmer MP. Grain-growth kinetics for alumina in the absence of a liquid phase. J Am Ceram Soc. 1985;68(1):C-22–C-24.
44. Berry KA, Harmer MP. Effect of MgO solute on microstructure development in Al_2O_3. J Am Ceram Soc. 1986;69(2):143–9.
45. Shaw NJ, Brook RJ. Structure and grain coarsening during the sintering of alumina. J Am Ceram Soc. 1986;69(2):107–10.
46. Greskovich C, Brewer JA. Solubility of magnesia in polycrystalline alumina at high temperatures. J Am Ceram Soc. 2001;84(2):420–5.
47. Bennison SJ, Harmer MP. Effect of magnesia solute on surface diffusion in sapphire and the role of magnesia in the sintering of alumina. J Am Ceram Soc. 1990;73(4):833–7.
48. Rhamdhani MA, Soepriyanto S, Ramelan A, Barliansyah A. Determination of mechanism and grain growth kinetics of MgO doped Al_2O_3. J Trop Med. 2005;12(3):148–58.
49. Lin FJT, De Jonghe LC. Initial coarsening and microstructural evolution of fast-fired and MgO-doped Al_2O_3. J Am Ceram Soc. 1997;80(11):2891–6.
50. Kottada RS, Chokshi AH. The high temperature tensile and compressive deformation characteristics of magnesia doped alumina. Acta Mater. 2000;48(15):3905–15.
51. Yoshizawa Y, Sakuma T. Improvement of tensile ductility in high-purity alumina due to magnesia addition. Scanning. 1992;40(11):2943–50.
52. Backhaus-Ricoult M, Guerin V, Huntz A-M, Urbanovich VS. High-temperature oxidation behavior of high-purity α-, β-, and mixed silicon nitride ceramics. J Am Ceram Soc. 2002;85(2):385–92.
53. Raider SI, Flitsch R, Aboaf JA, Pliskin WA. Surface oxidation of silicon nitride films. J Electrochem Soc. 1976;123(4):560–5.
54. Narushima T, Goto T, Hirai T, Iguchi Y. High-temperature oxidation of silicon carbide and silicon nitride. Mater Trans JIM. 1997;38(10):821–35.
55. Andrews P, Riley FL. The microstructure and composition of oxide films formed during high temperature oxidation of a sintered silicon nitride. J Eur Ceram Soc. 1989;5(4):245–56.
56. Zhou Y, Hyuga H, Kusano D, Yoshizawa Y, Hirao K. A tough silicon nitride ceramic with high thermal conductivity. Adv Mater. 2011;23(39):4563–7.
57. Fukuda S, Shimada K, Izu N, Miyazaki H, Iwakiri S, Hirao K. Crack generation in electroless nickel plating layers on copper-metallized silicon nitride substrates during thermal cycling. J Mater Sci Mater Electron. 2017;28(11):8278–85.

58. Hirao K, Fukuda S, Miyazaki H, Zhou Y, Hyuga H, Iwakiri S. Evaluation of residual thermal stress in Cu metalized silicon nitride substrates by Raman spectroscopy. In: 2018 International Conference on Electronics Packaging and iMAPS All Asia Conference (ICEP-IAAC) [Internet]. 2018. p. 194–6. https://doi.org/10.23919/ICEP.2018.8374701
59. Kim S, Gislason JJ, Morton RW, Pan XQ, Sun HP, Laine RM. Liquid-feed flame spray pyrolysis of nanopowders in the alumina-titania system. Chem Mater. 2004;16(12):2336–43.
60. Kim M, Laine RM. One-step synthesis of core-shell $(Ce_{0.7}Zr_{0.3}O_2)_x(Al_2O_3)_{1-x}$ $[(Ce_{0.7}Zr_{0.3}O_2)@Al_2O_3]$ nanopowders via liquid-feed flame spray pyrolysis (LF-FSP). J Am Chem Soc. 2009;131(26):9220–9.
61. Kim M, Hinklin TR, Laine RM. Core-shell nanostructured nanopowders along $(CeO_x)_x(Al_2O_3)_{1-x}$ tie-line by liquid-feed flame spray pyrolysis (LF-FSP). Chem Mater. 2008;20(16):5154–62.
62. Laine RM, Marchal J, Sun H, Pan XQ. A new $Y_3Al_5O_{12}$ phase produced by liquid-feed flame spray pyrolysis (LF-FSP). Adv Mater. 2005;17(7):830–3.
63. Wei GC, Rhodes WH. Sintering of translucent alumina in a nitrogen–hydrogen gas atmosphere. J Am Ceram Soc. 2000;83(7):1641–8.

SUPPORTING INFORMATION

Additional supporting information may be found online in the Supporting Information section.

How to cite this article: Zhang X, Cheng X, Jansohn M, et al. *t*-ZrO_2 toughened Al_2O_3 free-standing films and as oxidation mitigating thin films on silicon nitride via colloidal processing of flame made nanopowders (NPs). *J Am Ceram Soc*. 2021;104:1281–1296. https://doi.org/10.1111/jace.17570